

Coherent anti-Stokes Raman scattering hyperspectral tissue imaging with a wavelength-swept system

Steve Bégin,^{1,2} Bryan Burgoyne,³ Vincent Mercier,³
Alain Villeneuve,³ Réal Vallée,² and Daniel Côté^{1,2,*}

¹Centre de Recherche Université Laval Robert-Giffard (CRULRG), Université Laval,
Québec, QC, G1J 2G3, Canada

²Centre d'Optique, Photonique et Laser (COPL), Université Laval,
Québec, QC, G1V 0A6, Canada

³Genia Photonics Inc., 1111 Lapierre St., Lasalle, QC, H8N 2J4, Canada

*daniel.cote@crulrg.ulaval.ca

Abstract: We present a wavelength-swept coherent anti-Stokes Raman scattering (WS-CARS) spectroscopy system for hyperspectral imaging in thick tissue. We use a strategy where the Raman lines are excited sequentially, circumventing the need for a spectrometer. This fibre laser system, consisting of a pump laser synchronized with a rapidly tunable programmable laser (PL), can access Raman lines over a significant fraction of the high wavenumber region ($2700\text{--}2950\text{ cm}^{-1}$) at rates of up to 10,000 spectral points per second. To demonstrate its capabilities, we have acquired WS-CARS spectra of several samples as well as images and hyperspectral images (HSI) of thick tissue both in forward and epi-detection. This instrument should be especially useful in providing local biochemical information with surrounding context supplied by imaging.

© 2011 Optical Society of America

OCIS codes: (170.3880) Medical and biological imaging; (300.6230) Spectroscopy, coherent anti-Stokes Raman scattering; (180.4315) Nonlinear microscopy.

References and links

1. C. Kendall, M. Isabelle, F. Bazant-Hegemark, J. Hutchings, L. Orr, J. Babrah, R. Baker, and N. Stone, "Vibrational spectroscopy: a clinical tool for cancer diagnostics," *Analyst* **134**(6), 1029–45 (2009).
2. C. Krafft, G. Steiner, C. Beletes, and R. Salzer, "Disease recognition by infrared and Raman spectroscopy," *J. Biophoton.* **2**(1-2), 13–28 (2009).
3. M. D. Duncan, J. Reintjes, and T. J. Manuccia, "Scanning coherent anti-Stokes Raman microscope," *Opt. Lett.* **7**(8), 350–352 (1982).
4. A. Zumbusch, G. R. Holtom, and X. S. Xie, "Three-dimensional vibrational imaging by coherent anti-Stokes Raman scattering," *Phys. Rev. Lett.* **82**(20), 4142–4145 (1999).
5. C. L. Evans, E. O. Potma, M. Puoris'haag, D. Côté, C. P. Lin, and X. S. Xie, "Chemical imaging of tissue in vivo with video-rate coherent anti-Stokes Raman scattering microscopy," *Proc. Natl. Acad. Sci. U.S.A.* **102**(46), 16,807–16,812 (2005).
6. F. Ganikhanov, S. Carrasco, X. S. Xie, M. Katz, W. Seitz, and D. Kopf, "Broadly tunable dual-wavelength light source for coherent anti-Stokes Raman scattering microscopy," *Opt. Lett.* **31**(9), 1292–1294 (2006).
7. E. O. Potma, D. J. Jones, J.-X. Cheng, X. S. Xie, and J. Ye, "High-sensitivity coherent anti-Stokes Raman scattering microscopy with two tightly synchronized picosecond lasers," *Opt. Lett.* **27**(13), 1168–1170 (2002).
8. C. L. Evans, E. O. Potma, and X. S. Xie, "Coherent anti-Stokes Raman scattering spectral interferometry: determination of the real and imaginary components of nonlinear susceptibility $\chi^{(3)}$ for vibrational microscopy," *Opt. Lett.* **29**(24), 2923–2925 (2004).

9. E. Bélanger, S. Bégin, S. Laffray, Y. De Koninck, R. Vallée, and D. C. Côté, "Quantitative myelin imaging with coherent anti-Stokes Raman scattering microscopy: alleviating the excitation polarization dependence with circularly polarized laser beams," *Opt. Express* **17**(21), 18,419–18,432 (2009).
10. C. L. Evans and X. S. Xie, "Coherent Anti-Stokes Raman Scattering Microscopy: Chemical Imaging for Biology and Medicine," *Annu. Rev. Anal. Chem.* **1**(1), 883–909 (2008).
11. J.-X. Cheng, A. Volkmer, L. D. Book, and X. S. Xie, "Multiplex coherent anti-stokes Raman scattering microscopy and study of lipid vesicles," *J. Phys. Chem. B* **106**(34), 8493–8498 (2002).
12. M. Muller and J. M. Schins, "Imaging the thermodynamic state of lipid membranes with multiplex CARS microscopy," *J. Phys. Chem. B* **106**(14), 3715–3723 (2002).
13. R. Selm, M. Winterhalder, A. Zumbusch, G. Krauss, T. Hanke, A. Sell, and A. Leitenstorfer, "Ultrabroadband background-free coherent anti-Stokes Raman scattering microscopy based on a compact Er: fiber laser system," *Opt. Lett.* **35**(19), 3282–4 (2010).
14. T. W. Kee and M. T. Cicerone, "Simple approach to one-laser, broadband coherent anti-Stokes Raman scattering microscopy," *Opt. Lett.* **29**(23), 2701–2703 (2004).
15. A. F. Pegoraro, A. Ridsdale, D. J. Moffatt, Y. Jia, J. P. Pezacki, and A. Stolow, "Optimally chirped multimodal CARS microscopy based on a single Ti:sapphire oscillator," *Opt. Express* **17**(4), 2984–2996 (2009).
16. W. Langbein, I. Rocha-Mendoza, and P. Borri, "Single source coherent anti-Stokes Raman microspectroscopy using spectral focusing," *Appl. Phys. Lett.* **95**(8), 081109 (2009).
17. B. Chen, J. Sung, and S. Lim, "Chemical imaging with frequency modulation coherent anti-Stokes Raman scattering microscopy at the vibrational fingerprint region," *J. Phys. Chem. B* **114**(50), 16871–16880 (2010).
18. B. Burgoyne and A. Villeneuve, "Programmable lasers: design and applications," in *Society of Photo-Optical Instrumentation Engineers (SPIE) Conference Series*, vol. 7580 of *Society of Photo-Optical Instrumentation Engineers (SPIE) Conference Series*, pp. 758,002–758,002–15 (2010).
19. S. Li and K. T. Chan, "Electrical wavelength-tunable actively mode-locked fiber ring laser with a linearly chirped fiber Bragg grating," *IEEE Photon. Technol. Lett.* **10**(6), 799–801 (1998).
20. M. Balu, G. Liu, Z. Chen, B. J. Tromberg, and E. O. Potma, "Fiber delivered probe for efficient CARS imaging of tissues," *Opt. Express* **18**(3), 2380–2388 (2010).
21. T. A. Pologruto, B. L. Sabatini, and K. Svoboda, "ScanImage: flexible software for operating laser scanning microscopes," *Biomed. Eng.* **2**(1), 13 (2003).
22. J.-X. Cheng, A. Volkmer, L. D. Book, and X. S. Xie, "An epi-detected coherent anti-stokes raman scattering (E-CARS) microscope with high spectral resolution and high sensitivity," *J. Phys. Chem. B* **105**(7), 1277–1280 (2001).
23. P. D. Chowdary, W. A. Benalcazar, Z. Jiang, D. M. Marks, S. A. Boppart, and M. Gruebele, "High speed nonlinear interferometric vibrational analysis of lipids by spectral decomposition," *Anal. Chem.* **82**(9), 3812–8 (2010).
24. C. W. Freudiger, W. Min, B. G. Saar, S. Lu, G. R. Holtom, C. He, J. C. Tsai, J. X. Kang, and X. S. Xie, "Label-free biomedical imaging with high sensitivity by stimulated Raman scattering microscopy," *Science* **322**(5909), 1857–1861 (2008).
25. K. Wang, C. W. Freudiger, J. H. Lee, B. G. Saar, X. S. Xie, and C. Xu, "Synchronized time-lens source for coherent Raman scattering microscopy," *Opt. Express* **18**(23), 24019–24024 (2010).

1. Introduction

Raman based spectroscopy techniques are highly sensitive to the biochemical nature of materials and have the high spatial resolution associated with optical microscopy. Fast identification of biochemical components in turbid materials has generated strong interest in live tissue spectroscopy since it makes disease diagnosis possibly achievable *in situ*. For example, the diagnostic potential of Raman spectroscopy has generated a large amount of literature in oncology alone [1,2]. However, it has become clear that a clinically useful technique should also provide context for diagnosis through imaging, something impossible with low sensitivity techniques such as spontaneous Raman spectroscopy.

Coherent anti-Stokes Raman scattering [3, 4] is a nonlinear technique with the necessary sensitivity for fast chemically-specific imaging. It requires two or more laser pulses of different wavelengths to coherently excite a Raman active vibrational mode in a molecule. On the one hand, the nonlinear nature of the process demands short pulses (ps or fs) with high peak power, and on the other hand a system with good tunability or a large bandwidth is necessary for spectroscopic measurements. Typical CARS systems based on optical parametric oscillators [5, 6] or synchronized Ti:Sapphire lasers [7,8] have been successful for imaging lipids, myelin and

water [4, 9] (for a review see [10]) but their relatively slow tunability has hampered their use in spectroscopy. Broadband methods based on transform-limited ultrashort pulses [11–13] or continuum generation [14] have been successful for spectral imaging of optically thin systems. However, their need for a spectrometer to resolve the vibrational spectra results in very poor collection efficiency in turbid materials such as tissue where diffusion is important. Methods using spectral focussing of broadband excitation pulses avoid the need for a spectrometer but rely on a mechanical delay line for vibrational tuning [15–17].

We propose a strategy where the Raman lines are excited sequentially at very high speed by narrowband picosecond pulses. The wavelength-swept coherent anti-Stokes Raman scattering system presented here is based on a master oscillator power amplifier (MOPA) pump laser synchronized with a rapidly tunable programmable laser (PL) as the Stokes beam. The spectral bandwidth of this instrument covers most of the high wavenumber region ($2700\text{--}2950\text{ cm}^{-1}$). This strategy has many advantages compared to other existing methods. With the spectroscopic information encoded in time (Fig. 1(a)), the detection can be done using fast and sensitive photomultiplier tubes. This is especially important for CARS spectroscopy in thick tissue where the large étendue of the scattered signal is not compatible with the small entrance slit of spectrometers, resulting in poor collection efficiencies. Furthermore, this system allows random access to any Raman line within its bandwidth. Since the acquisition time scales linearly with the number of spectral points, this should prove to be an essential feature for applications where speed is critical. Finally, the high flexibility of the wavelength sweep rate can easily accommodate rapid single point spectroscopy or hyperspectral imaging where a whole image is acquired for every Raman line (Fig. 1(b)). In this manuscript, we use the system for WS-CARS spectroscopy as well as single-line and hyperspectral imaging in thick tissue both in forward and epi-detection.

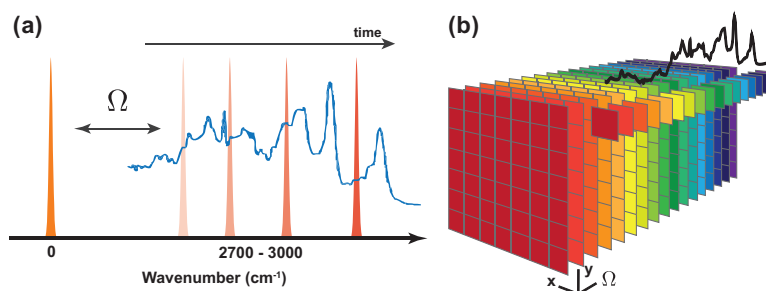


Fig. 1. (a) In wavelength-swept CARS spectroscopy, the Raman vibrations (Ω) are excited sequentially and the spectroscopic information is encoded in time. (b) Hyper spectral images are constructed by raster scanning of the sample for every Raman line. Every pixel contains a CARS spectrum.

2. Materials and methods

2.1. Synchronized fibre lasers system

The synchronized fibre lasers system presented here has characteristics tailored specifically for CARS spectroscopy and hyperspectral imaging. The system is composed of a programmable laser [18] and a MOPA driven by high-speed low-jitter electronics (Fig. 2(a)). The key characteristic of this system is the ability of the PL to rapidly (up to 10 kHz) and arbitrarily access any wavelength in its tuning range while maintaining synchronization with the MOPA. The novel programmable laser is based on a dispersion-tuned, actively mode-locked scheme [19]. The dispersive elements are four chirped fibre Bragg gratings (CFBG) that essentially establish

different cavity lengths for each wavelength. As a consequence, the laser operates at different repetition rates depending on the wavelength. Tuning is achieved by changing the driving frequency of the electro-optic modulator (EOM) (Fig. 2(b)). The tuning range of the PL goes from 1524 nm (12.35 MHz) to 1608.6 nm (13.98 MHz) in steps of 0.1 nm that match the spectral line widths of the laser pulses. The modulator is driven by a 25 picosecond pulse generator triggered by the function generation circuit. A wavelength division multiplexer (WDM) is used to combine the 980 nm pump and the signal into the erbium-doped fibre. The PL is amplified up to an average power of 35 mW using an erbium-doped amplifier. The MOPA is based on a 1080 nm CW laser diode externally modulated through an EOM driven by a 25 ps pulse generator. The optical signal is filtered and subjected to three stages of amplification resulting in nominally 100 mW of average power. We note that although every wavelength of the PL has a different repetition rate it does not pose a synchronization problem since both the MOPA and the PL are driven by the same function generation electronics including an arbitrary electronic time delay. Since the delay between the pulse trains is controlled electronically, there is no need for a mechanical delay line in the microscope optical path. Both lasers generate optical pulse widths of less than 35 ps, corresponding to a CARS excitation line width of less than 0.5 cm^{-1} . The long pulses (nominally 6 times longer than ideal picosecond CARS sources) are more than compensated for by the lower repetition rate (nominally 8 times lower than high repetition rate systems) yielding peak power (or pulse energy) on the order of 240 W (8 nJ) and 85 W (3 nJ) for the MOPA and PL respectively.

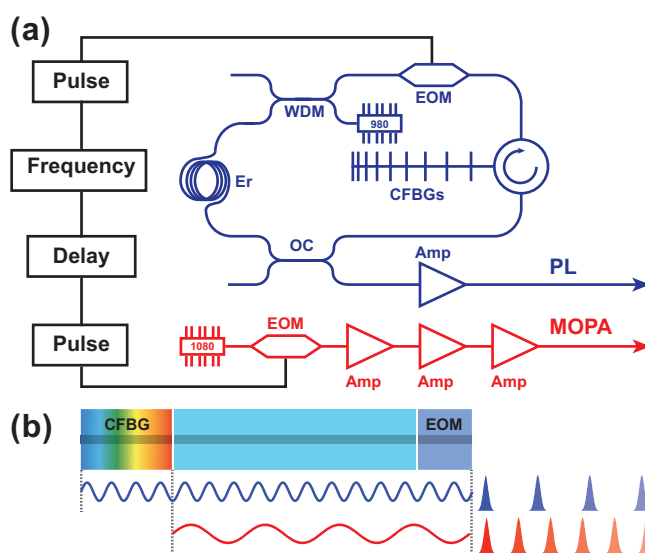


Fig. 2. (a) Schematic of the synchronized lasers. The PL (blue) and the MOPA (red) are driven by high-speed function generation electronics with adjustable delay (black). In the PL, the wavelength is determined by the frequency generator through dispersion tuning using four dispersive CFBGs and an EOM. The EOM is driven by a 25 picosecond pulse generator. A wavelength division multiplexer (WDM) is used to combine the 980 nm pump and the signal into the erbium-doped fibre. The MOPA consists of a CW laser diode modulated through an EOM by a 25 ps pulse generator with the same repetition rate as the PL. (b) The CFBG forms different cavity lengths for each wavelength. Tuning is achieved by changing the driving frequency of the EOM, and consequently the repetition rate of the laser.

2.2. Experimental setup description

A schematic diagram of the experimental layout is shown in Fig. 3. The pump and Stokes beams from the synchronized lasers are collimated independently in order to prevent two-beams nonlinear interactions [20], and recombined using a long-pass filter at 45° (Semrock, LP02-1319RS-25). The beams are sent to a homemade laser-scanning microscope which collects non-descanned light in both forward- and epi-direction configurations. A gold coated 52X/0.65NA reflecting objective optimized for IR light with cover slip correction ($140\ \mu\text{m}$) is used for imaging (Edmund Optics, 25-0548-020). This objective does not suffer from material absorption since gold has a very good reflectivity in the near IR ($R > 98\%$) but is minimally affected by obscuration (16.7%) due to the Cassegrain design. Furthermore, it is free from chromatic aberration. The optical power at the sample is 40 mW and 15 mW for the pump and Stokes beams respectively ($\sim 40\%$ of the laser output power). The forward generated CARS signal is collected by a 40X/0.8NA water immersion objective (Olympus, LUMPlanFI/IR), while the epi-detected signals returns through the illumination objective. Both forward and epi CARS signals are extracted by long-pass filters used at 45° (Semrock, LP02980R-25) and filtered using combinations of two bandpass filters (Semrock, FF01-832/37-25 and Chroma, ET801/90m) before being detected by photomultiplier tubes (PMT) detectors (Hamamatsu, R3896). A homemade data acquisition system implemented in Matlab is used for WS-CARS spectroscopy experiments. ScanImage [21] is used for imaging and HSI experiments. For the system characterization experiments, a broadband 50/50 beam splitter is inserted in the beam path to send part of the excitation beams to a BBO crystal for sum frequency generation (SFG). The filtered (Semrock, FF01-640/14-25) SFG signal is measured using a silicon photodiode (Thorlabs, PDA36A).

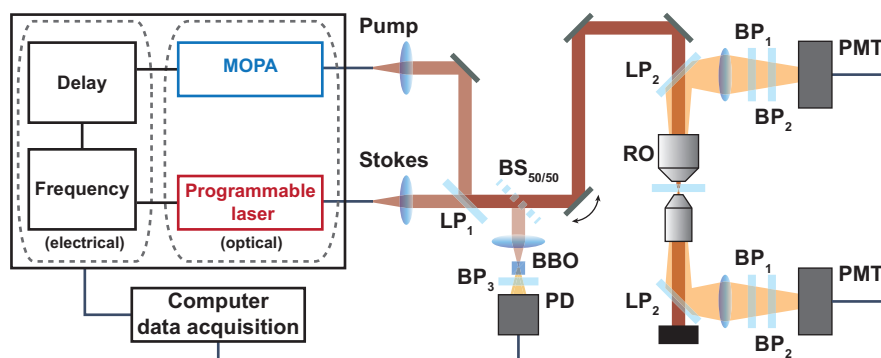


Fig. 3. WS-CARS microscopy setup. Pulses from the synchronized lasers are collimated separately, combined with a long-pass filter (LP_1) and then routed to a homemade laser scanning microscope. The beams are focused on the sample using a 52X/0.65NA reflecting objective (RO). The CARS signal is extracted with long-pass filters (LP_2), filtered using bandpass filters (BP_1 , BP_2) and detected with PMTs in the epi- and forward- directions. A beam splitter ($BS_{50/50}$) can be inserted in the path for characterization experiments. The SFG generated in a BBO crystal is filtered (BP_3) and detected using a photodiode (PD).

2.3. Synchronized lasers system optimization and characterization

For every wavelength of the PL, the dispersion resulting from the laser cavities and the additional optics in the setup has to be electronically compensated to ensure temporal overlap of the pulses from both lasers at the sample. The function generation electronics triggering the lasers provide an adjustable time delay between both pulse trains. It can be tuned with high res-

olution delay increments (16 bits) throughout the large dynamic range of one round trip time. For example, the delay resolution at 12 MHz (83.3 ns of round trip time) is 1.27 ps. In order to optimize the temporal superposition of the pulse trains, SFG is performed in a BBO crystal. The SFG signal is recorded while the time delay between the PL and the MOPA is swept at high speed (Fig. 4(a)). The optimal time delays are compiled in a lookup table that is used to automatically adjust the electronic delay when the PL wavelength is changed. Since the delay is controlled electronically, this can be done very rapidly (~ 10 ms/sweep) and in an automated fashion. The SFG delay curves are the cross-correlation of the pulses from both lasers [7]. For example, the 50 ps FWHM of the cross-correlation in Fig. 4(a) corresponds to about 35 ps for both laser pulses. This result is confirmed by the autocorrelation of the MOPA pulses (not shown). The pulse widths of the PL remain constant across the whole tuning range except for a slight broadening caused by a lower gain at the upper end of the range. The inset shows the SFG signal fluctuations at the half-maximum time delay over the course of 60 seconds. Since these fluctuations are due to both the timing jitter and power fluctuations in the MOPA and PL, we can set an upper limit of 2.4 ps on the timing jitter from the measurement. The signal is measured through a 1.9 MHz low-pass filter and sampled at 5 MHz to avoid aliasing problems and averaged over 1 ms.

The key feature of this system is its ability to rapidly and arbitrarily change the wavelength difference between the two lasers while maintaining synchronization and temporal overlap at the sample. This is demonstrated in Fig. 4(b) which shows wavelength sweeps for 3 different tuning rates (20 $\mu\text{s}/\text{step}$, 100 $\mu\text{s}/\text{step}$ and 1 ms/step). The resulting SFG spectra cover the whole 84 nm tuning range with a resolution of 1 nm. SFG is a better indicator of CARS efficiency than average laser power since it depends directly on the nonlinear mixing of the pulses as can be seen by comparing SFG (lines) and PL power spectra (black diamonds). The SFG signal level is constant from 1525 nm to 1560 nm and then progressively drops due to the lower gain of the PL amplifier at higher wavelengths as well as inefficiencies of the BBO crystal. This will translate into lower CARS efficiencies for spectroscopy at longer wavelengths, as will be shown in Fig. 6 and 7. The sweep consistency is maintained as the sweeping rate increases, showing only some slight variations at 100 $\mu\text{s}/\text{step}$ and some degradation at 20 $\mu\text{s}/\text{step}$. At rates of 1 ms/step and slower, the shapes of the spectra are identical and highly repeatable. The ripples in the spectra are caused by the transfer function of the PL optical components, especially the chirped fibre Bragg gratings.

Figure 4(c) shows a typical SFG time series (blue) highlighting the PL cavity dynamics following wavelength changes at 50 $\mu\text{s}/\text{step}$ (black). The actively mode-locked operation is usually established in 15 μs (red) but may require more time at longer wavelengths near the end of the tuning range. For this reason, we operate the PL at tuning rates of 100 $\mu\text{s}/\text{step}$ or slower, discarding the first 15 μs of acquired data. This dead time is a result from the erbium-doped fibre gain dynamics and could be overcome using other gain media such as semiconductor optical amplifiers.

Figure 4(d) shows an epi-CARS image of a thin-film interface of water (which does not contain C-H bonds) and peanut oil acquired at 2850 cm^{-1} (PL tuned to 1560 nm). The 4% signal-to-background ratio from the average line profile yields an upper limit to the nonresonant background contribution. In fact, most of the background signal comes from the PMT dark noise and a small leakage of the pump laser through the optical filters. This small nonresonant contribution is explained by the 35 ps pulse length [22], since the non-resonant background decreases for increasing pulse widths.

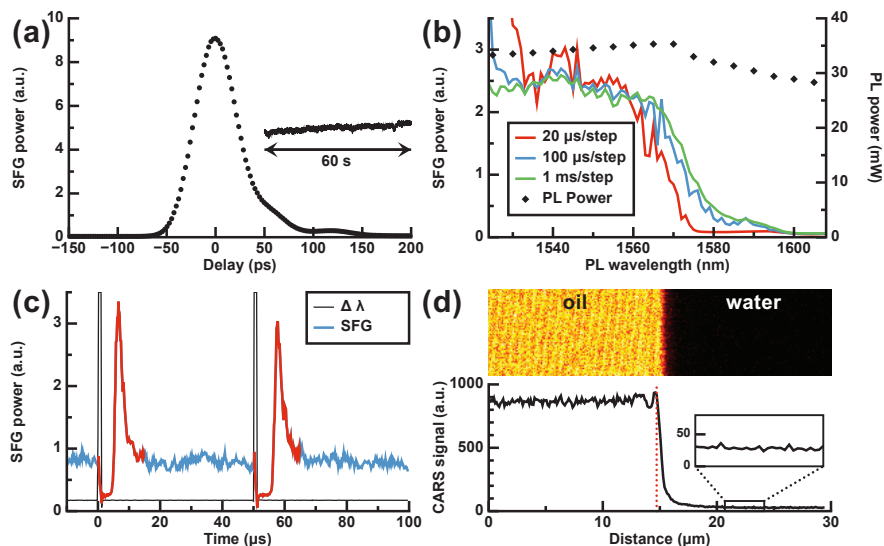


Fig. 4. (a) Typical cross-correlation trace between the PL and the MOPA, used to calibrate the temporal overlap of the pulses at the target and to characterize their pulse widths. The delay sweep acquired at a rate of $50 \mu\text{s}/\text{step}$ ($\lambda_{PL} = 1560 \text{ nm}$, total time = 7.5 ms). Inset shows the half maximum SFG signal recorded over 60 seconds. (b) SFG spectra acquired at different sweep rates are highly repeatable. The diamond curve indicates the power spectrum of the PL. (c) SFG time series (blue) reveals the PL cavity dynamics following wavelength changes (black). The stabilization period (red) typically lasts $15 \mu\text{s}$. (d) CARS image of the interface of a water-oil thin film indicates that the non-resonant background is at most 4%.

3. Results and discussion

3.1. CARS imaging

The imaging capabilities of the WS-CARS microscope are demonstrated on a mouse ear. The adipocytes are clearly visible in both the forward- (Fig. 5(a)) and epi-detected (Fig. 5(b)) images. This epi-detection capability is a direct consequence of the wavelength-swept strategy that removes the necessity of using a spectrometer for collection and permits an efficient collection of all the CARS photons with a large area PMT. The anti-Stokes signal in the images comes from the symmetric CH_2 stretching mode of the lipids present in the structures approximately $80 \mu\text{m}$ deep in the skin. The images are an average intensity projection of 10 frames acquired in a total of 7.5 seconds.

3.2. WS-CARS spectroscopy

The wavelength-sweep mode is used for single point spectroscopy by rapidly tuning the PL and recording the anti-Stokes signal. The maximum spectral resolution of the system is given by the CARS excitation line width of less than 0.5 cm^{-1} and the matching minimal tuning step of 0.4 cm^{-1} . Typical Raman line widths in the high wavenumber region are on the order of several tens of cm^{-1} . Hence, the tuning step in the experiments can be adjusted without any loss of information.

In Fig. 6(a), WS-CARS spectra of different chemical species (peanut oil, dimethyl sulfoxide (DMSO), silicone and polystyrene) are presented. The spectral asymmetry in nonlinear effi-

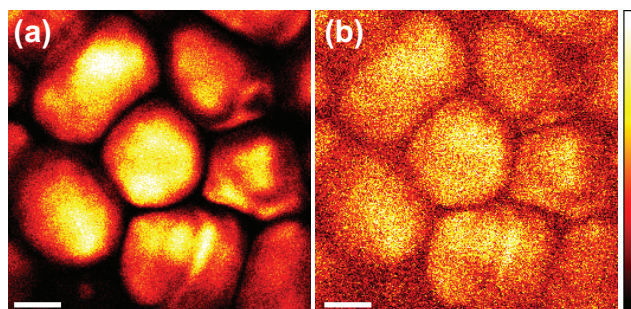


Fig. 5. *Ex vivo* CARS images of adipocytes in a 1-mm-thick mouse ear acquired in the forward- (a) and epi- (b) direction at 2849 cm^{-1} . The signal in image (a) is approximately 6 times brighter than (b). The images are an average of 10 frames acquired in a total of 7.5 seconds. Scale bars are $20\text{ }\mu\text{m}$.

ciency from this laser system (see Fig. 4(b)) modulates the intensities of the Raman lines but not their spectral positions. Peanut oil is composed mainly of unsaturated fatty acid (56.6% oleic acid and 26.7% linoleic acid). Its Raman band, attributed to the symmetric CH_2 stretching mode, shows a strong peak at 2849 cm^{-1} . Pure DMSO has an intense Raman band at 2914 cm^{-1} attributed to the symmetric CH_3 stretching vibrations of its methyl groups. Silicone and polystyrene have slightly more complex spectra which are also weaker. The liquid samples are placed in a $140\text{ }\mu\text{m}$ deep chamber on a microscope slide and covered by a cover slip. A mixture of $10\text{ }\mu\text{m}$ polystyrene beads (Polysciences) and water is used in a similar manner. Proper alignment of the excitation beams on a polystyrene bead is done using a CARS image such as the one presented in Fig. 6(b). All the spectra are acquired in 622 ms at a rate of 2 ms/step. They cover the range from 2697.6 to 2954.1 cm^{-1} with an acquisition resolution of 0.8 cm^{-1} (321 points). Figure 6(b) shows two images of $10\text{ }\mu\text{m}$ diameter polystyrene beads in peanut oil recorded at two different Raman lines. The image acquired at 2849.0 cm^{-1} (top) emphasizes the contribution from the surrounding oil while the image acquired at 2889.8 cm^{-1} (bottom) highlights the equal contributions of the polystyrene and the oil at that wavenumber. The images are an average intensity projection of 10 frames acquired in a total of 7.5 seconds.

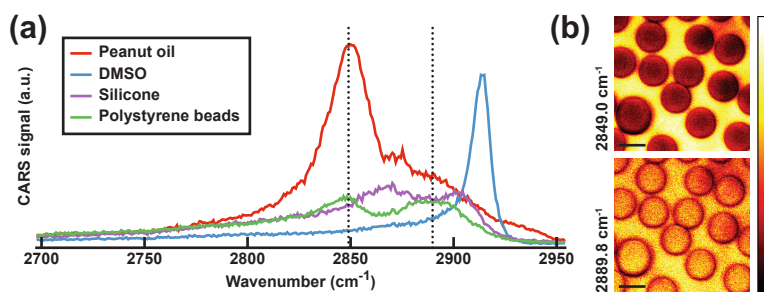


Fig. 6. (a) WS-CARS spectra of peanut oil (red), DMSO (blue), silicone (purple) and polystyrene beads (green). Each spectrum ranges from 2697.6 to 2954.1 cm^{-1} with a resolution of 0.8 cm^{-1} . The PL tuning rate is 2 ms/step and the total acquisition time is 622 ms per spectrum. (b) CARS images of polystyrene beads in peanut oil recorded at 2849.0 cm^{-1} (top) and 2889.8 cm^{-1} (bottom) in the forward direction. Scale bars are $10\text{ }\mu\text{m}$.

Next, the sensitivity and speed of the single point spectroscopy mode is demonstrated. Figure 7 shows WS-CARS spectra of various fatty acids of different degrees of saturation. Fatty

acids are characterized by a carboxylic acid ($R\text{-COOH}$) attached to an aliphatic chain ($\dots\text{-CH}_2\text{-CH}_2\text{-CH}_2\text{-}\dots$) which can be saturated or unsaturated to various degrees. The degree of unsaturation can be determined based on their nonlinear Raman signature [23]. As seen in Fig. 7 the number of double bonds in the chain alters the relative shape of the spectra. The spectra are in good agreement with previously published spontaneous Raman spectra [24]. Olive oil, composed mostly of oleic acid and palmitic acid, is 13% saturated, 73% monounsaturated and 11% polyunsaturated. The other fatty acids are docosahexaenoic acid (DHA), eicosapentaenoic acid (EPA) and arachidonic acid (AA) which have respectively six, five and four C=C bonds in their aliphatic chains. The samples are placed in a $140\ \mu\text{m}$ deep chamber on a microscope slide and protected by a cover slip. Each spectrum ranging from 2697.6 to $2989.7\ \text{cm}^{-1}$ with an acquisition resolution of $0.4\ \text{cm}^{-1}$ (711 points), is acquired in 71 ms at a rate of $100\ \mu\text{s}/\text{step}$. The data is filtered using a running average algorithm with a window of 11 pixels for an effective resolution of $4\ \text{cm}^{-1}$.

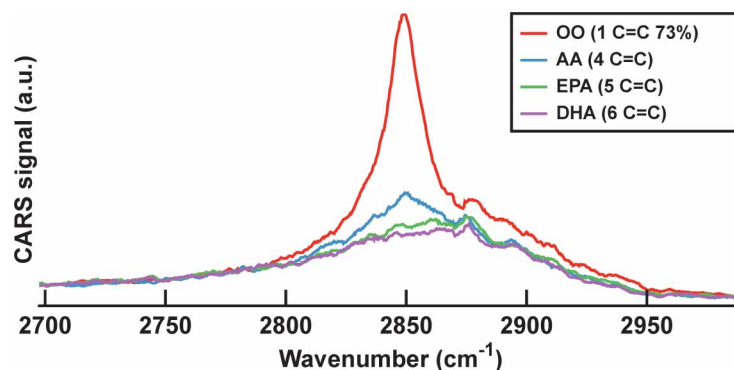


Fig. 7. WS-CARS spectra of unsaturated fatty acids. Olive oil (OO) is 13% saturated and 73% monounsaturated, arachidonic acid (AA) has 4 double bonds, eicosapentaenoic acid (EPA) has 5 double bonds and docosahexaenoic acid (DHA) has 6 double bonds. Each spectrum was acquired in 71 ms at a rate of $100\ \mu\text{s}/\text{step}$.

3.3. WS-CARS hyperspectral imaging

In this section, hyperspectral imaging of a skin sample incubated in DMSO (Fig. 8) is presented. DMSO is a lipophobic compound that easily penetrates the skin. For this experiment, a complete mouse ear is kept in DMSO for 2 hours at room temperature and placed on a microscope slide for imaging. The HSI is acquired using ScanImage externally triggered by the synchronized lasers system during a wavelength sweep ranging from $2786.8\ \text{cm}^{-1}$ to $2950.1\ \text{cm}^{-1}$ with a resolution of $2\ \text{cm}^{-1}$ at a rate of 1 Hz. The acquisition time for the $256 \times 256 \times 81$ HSI is 81 seconds (1.2 ms per spectrum) with a corresponding true pixel dwell time of $6.4\ \mu\text{s}$ per wavelength. This pixel dwell time is comparable to what is achieved using commercial systems, and emphasizes that the system is almost as efficient as fluorescence microscopes while providing full spectral information. A closer look at the HSI shows that the fat is compartmentalized in the adipocytes (Fig. 8 left image, $2849\ \text{cm}^{-1}$) while the DMSO is constrained to the extracellular space (Fig. 8 right image, $2914\ \text{cm}^{-1}$). The lipophobic nature of DMSO is also evident in the spectral projection (Fig. 8 central panel) where we can see that the two compounds are mutually exclusive.

Discrimination between chemical species can be done much more rapidly by imaging only the relevant Raman bands since the integration time scales linearly with their numbers. For example, a look at the spectra from Fig. 8 shows that DMSO has a vibrational resonance

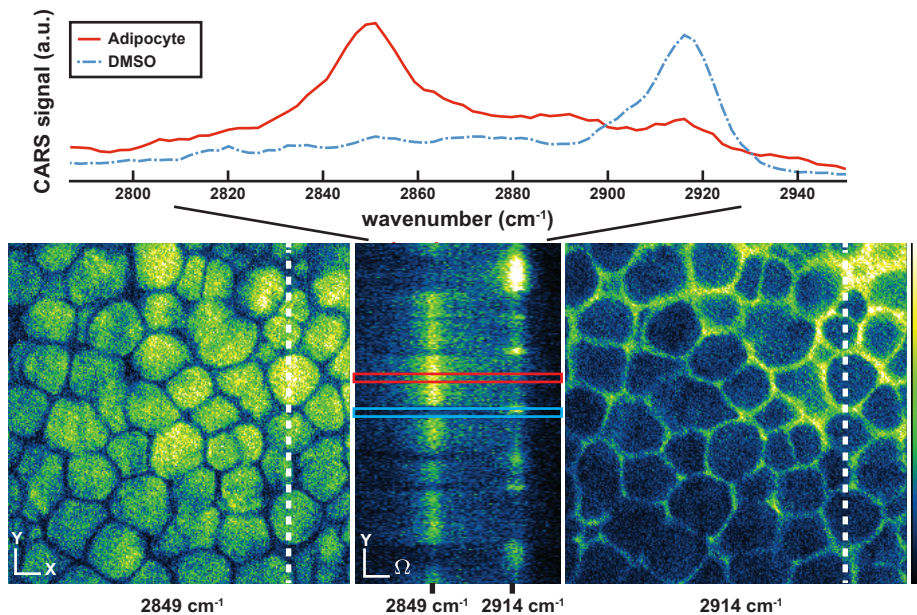


Fig. 8. Hyperspectral CARS images of mouse skin incubated in DMSO for 2 hours. The left and right images correspond to the lipid (2849 cm^{-1}) and DMSO (2914 cm^{-1}) Raman line. The central panel shows a spectral projection along the dotted lines. The adipocytes and DMSO CARS spectra (4-pixel-wide red and blue boxes in central panel) are shown on top. A total of 81 images were acquired at a rate of one frame per second. Every pixel in the HSI is a spectrum ranging from 2786.8 cm^{-1} to 2950.1 cm^{-1} . Acquisition time for the $256 \times 256 \times 81$ HSI is 81 seconds (1.2 ms per spectrum). The images were acquired in the forward direction. Scale bar is $10\text{ }\mu\text{m}$.

(2914 cm^{-1}) which is well separated from the lipid peak (2849 cm^{-1}). Therefore, they can be easily differentiated using random access multi line imaging resulting in much shorter acquisition times. Furthermore, since this system can access any arbitrary sequence of Raman lines in its tuning range, multi line imaging can easily be scaled to suit more demanding experiments. This will be especially useful for applications such as *in vivo* tissue diagnosis where many vibrational lines would be needed to identify complex tissue constituents with great speed. In this example, after proper identification of the diagnostically relevant Raman lines, imaging could be performed over a large area in a short time.

4. Conclusion

We presented a wavelength-swept approach to CARS microscopy that is especially well suited for experiments on thick tissue where scattering plays an important role. This system does not require a spectrometer that would limit collection efficiency and prevent epi-detection. The current system configuration is designed to access Raman lines within most of the high wavenumber region ($2700\text{--}2950\text{ cm}^{-1}$). Tuning speeds of up to $100\text{ }\mu\text{s}$ per spectral points are demonstrated with the acquisition of CARS spectra of various samples. As well, CARS hyperspectral images containing tens of thousands of spectra are acquired in just over a minute. Thanks to the 12 MHz repetition rate, efficient CARS generation is possible even with 35 ps pulses. Strategies to shorten the pulses, using for instance a shorter pulse generator or a time-lens [25], are being explored. This flexible all-fibre system could bridge an important gap between fundamental re-

search microscopy tools and clinically useful instruments by combining the context of imaging with the richness of spectroscopic information.

Acknowledgments

This research was funded by the Collaborative Health Research Program, the Canadian Institute for Photonics Innovation, the Fonds québécois de la recherche sur la nature et les technologies and the Canada Research Chair Program. The authors would like to acknowledge Stephane Pagès, Olivier Dupont-Thérien, Erik Bélanger and Joel Crépeau for helpful discussions.